

# FireFly-T: High-Throughput Sparsity Exploitation for Spiking Transformer Acceleration with Dual-Engine Overlay Architecture

Tenglong Li , Jindong Li , Guobin Shen , Dongcheng Zhao , Qian Zhang , Yi Zeng 

**Abstract**—Spiking transformers are emerging as a promising architecture that combines the energy efficiency of Spiking Neural Networks (SNNs) with the powerful attention mechanisms of transformers. However, existing hardware accelerators lack support for spiking attention, exhibit limited throughput in exploiting fine-grained sparsity, and struggle with scalable parallelism in sparse computation. To address these, we propose FireFly-T, a dual-engine overlay architecture that integrates a sparse engine for activation sparsity and a binary engine for spiking attention. In the sparse engine, we propose a high-throughput sparse decoder that exploits fine-grained sparsity by concurrently extracting multiple non-zero spikes. To complement this, we introduce a scalable load balancing mechanism with weight dispatch and out-of-order execution, eliminating bank conflicts to support scalable multidimensional parallelism. In the binary engine, we leverage the byte-level write capability of SRAMs to efficiently manipulate the 3D dataflows required for spiking attention with minimal resource overhead. We also optimize the core AND-PopCount operation in spiking attention through a LUT6-based implementation, improving timing closure and reducing LUT utilization on Xilinx FPGAs. As an overlay architecture, FireFly-T further incorporates an orchestrator that dynamically manipulates input dataflows with flexible adaptation for diverse network topologies, while ensuring efficient resource utilization and maintaining high throughput. Experimental results demonstrate that our accelerator achieves  $1.39\times$  and  $2.40\times$  higher energy efficiency, as well as  $4.21\times$  and  $7.10\times$  greater DSP efficiency, compared to FireFly v2 and the transformer-enabled SpikeTA, respectively. These results highlight its potential as an efficient hardware platform for spiking transformer.

**Index Terms**—Spiking Transformer, Fine-Grained Sparsity, Dual-Engine Overlay Architecture, Hardware Accelerator

arXiv:2505.12771v1 [cs.AR] 19 May 2025

Manuscript created 20 May 2025. This work is supported by a funding from Institute of Automation, Chinese Academy of Sciences (Grant No. E411230101). (Corresponding authors: Qian Zhang; Yi Zeng.)

Tenglong Li, and Jindong Li are with the School of Artificial Intelligence, University of Chinese Academy of Sciences, Beijing 100049, China. (e-mail: litenglong2023@ia.ac.cn; lijindong2022@ia.ac.cn).

Guobin Shen is with the School of Future Technology, University of Chinese Academy of Sciences, Beijing 100049, China; and the Center for Long-term AI, Beijing 101407, China. (e-mail: shengguobin2021@ia.ac.cn).

Dongcheng Zhao is with the Center for Long-term AI, Beijing 101407, China. (e-mail: zhaodongcheng2016@ia.ac.cn).

Qian Zhang is with the School of Artificial Intelligence, University of Chinese Academy of Sciences, Beijing 100049, China; and the Center for Long-term AI, Beijing 101407, China. (e-mail: q.zhang@ia.ac.cn).

Yi Zeng is with the Center for Long-term AI, Beijing 101407, China; and the State Key Laboratory of Brain Cognition and Brain-inspired Intelligence Technology, Chinese Academy of Sciences, Shanghai 200031, China (e-mail: yi.zeng@ia.ac.cn).

All authors are also with the Brain-inspired Cognitive AI Lab, Institute of Automation, Chinese Academy of Sciences, Beijing 100190, China.

## I. INTRODUCTION

TRANSFORMER networks have revolutionized domains such as natural language processing [1]–[3] and computer vision [4]–[6]. The Vision Transformer (ViT), for example, processes images as patch sequences and achieves state-of-the-art results [4]. Meanwhile, Spiking Neural Networks (SNNs), inspired by the biological brain [7], are drawing attention for their energy efficiency. This efficiency arises from their binary activations and inherently sparse computation, with studies showing that SNNs naturally exhibit high sparsity without the need for explicit pruning [8], [9], marking them as promising candidates for energy-efficient real-world applications.

Integrating these two paradigms, spiking transformers combine the powerful attention mechanism of transformers with the efficiency of SNNs, demonstrating competitive performance while reducing computational overhead and power consumption [10]–[16]. Further enhancements, such as binary attention mechanisms [17], [18], offer additional advantages by reducing bit-width of attention maps and potentially enhancing accuracy, solidifying spiking transformers as an attractive direction for practical deployment.

To fully unlock the potential of spiking transformers, the development of specialized hardware support is crucial—especially for accelerating spiking attention and effectively exploiting activation sparsity. While recent efforts have advanced SNN acceleration, existing solutions still exhibit limitations and fall short when applied to spiking transformers. Specifically, we identify three critical limitations in current hardware approaches, as detailed below:

**Inefficient Spiking Transformer Support.** Existing SNN accelerators primarily focus on optimizing multilayer perceptron (MLP) and convolutional layers [19]–[23], often neglecting the attention mechanism crucial to spiking transformers. Mapping attention operations onto existing hardware is challenging due to the unique dataflow patterns of the multi-head attention mechanism and inefficiencies arising from bit-width mismatches—spiking attention performs operations between 1-bit operands, whereas accelerators are optimized for spiking convolutions with 1-bit activations and multi-bit weights. Dedicated hardware designs for spiking attention also exhibit limited efficiency. As illustrated in Fig. 1A, Gao et al. [24] utilize six-input Look-Up Tables (LUT6) with only two active inputs for AND followed by Population Count (AND-PopCount) operations central to binary attention, resulting in suboptimal resource utilization. Fang et al. [25] adopt a  $3\times 3$

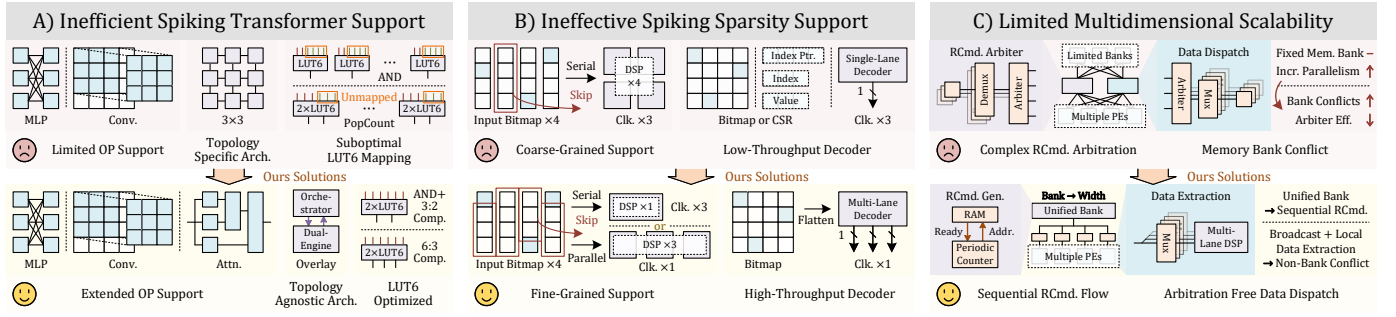


Fig. 1. Overview of major limitations in hardware acceleration for spiking transformers, alongside the proposed solutions and features of our FireFly-T.

core organization, which suffers from performance degradation across diverse network topologies, and also inefficiently accumulates 1-bit spikes through an 8-bit adder tree.

**Ineffective Spiking Sparsity Support.** Achieving high-throughput while effectively exploiting spiking sparsity remains a major challenge. Several prior studies have attempted to exploit coarse-grained sparsity [22], [25], which naturally leads to more regular dataflow and improved workload balance relative to fine-grained methods. However, this approach often results in suboptimal sparsity utilization. As depicted in Fig. 1B, under 75% uniform sparsity, grouping spikes in fours yields only a ~31% chance of skipping an entire group. This limits performance gains, while still requiring four DSPs per group and some of which remain idle when processing. On the other hand, while fine-grained methods are more effective at exploiting sparsity, they often suffer from low input processing throughput. Existing sparse accelerators that decode Compressed Sparse Row (CSR) or BitMap formats typically process only one non-zero activation per processing element (PE) per cycle [23], [26], leading to underutilized input bandwidth than dense or coarse-grained approaches [27].

**Limited Multidimensional Scalability.** Dense accelerators—such as DeepFire2 [28] and FireFly v2 [27]—benefit from regular dataflows that naturally enable extensive parallelism across multiple dimensions, including spatial, temporal, and channel dimensions in SNNs. However, this regularity comes at the cost of reduced energy efficiency when processing sparse inputs and limited inherent support for sparsity. In contrast, sparse accelerators face challenges in achieving comparable multidimensional parallelism. Their irregular dataflows and the resulting workload imbalances often limit parallelism to a narrower set of dimensions [22], [23]. A major contributing factor is the overhead introduced by sparsity management mechanisms. As shown in Fig. 1C, workload balancing techniques using crossbars [22], [29] can introduce severe memory bank conflicts caused by weight reuse—especially when scaling pixel- or temporal-level parallelism—which degrade throughput and limit overall performance scaling.

In this work, we present **FireFly-T**, an architecture designed to accelerate both spiking convolutional networks and spiking transformers. Extending our FireFly series, the *T* denotes enhanced transformer support. FireFly-T addresses the challenges outlined in Fig. 1 with its solutions depicted in the lower part. Our main contributions are summarized below:

- We propose a dual-engine overlay architecture featuring dedicated sparse and binary engines coupled with flexible orchestrator. This design enables efficient support for spiking transformers with latency-hiding pipelines and multidimensional parallelism, while sustaining high performance across diverse network topologies.
- We present a high-throughput sparse engine capable of effective fine-grained sparsity exploitation, incorporating multi-lane sparse decoders and a non-bank-conflict workload balancing mechanism. This contributes to comparable throughput while reducing DSP usage by 75% compared to FireFly v2, improving overall energy efficiency.
- We implement a resource-efficient binary engine featuring an implicit transpose mechanism, combined with LUT6-optimized AND-PopCount logic. This design eliminates the need for additional transposition buffers and reduces LUT utilization by 52%, enhancing overall resource efficiency for spiking attention support.

The remainder of this paper is organized as follows: Section II provides background on spiking attention and the structure of the spiking transformer. Section III introduces the fundamentals of FireFly-T. Section IV presents our proposed accelerator microarchitecture, including the sparse engine, binary engine, and orchestrator implementation. Section V describes the experimental setup and provides a comprehensive evaluation. Section VI reviews related work, and Section VII concludes the paper and outlines directions for future research.

## II. BACKGROUND

### A. Spiking Attention Mechanism

The attention mechanism is a core component of transformer architectures, generating context-aware representations by weighting value vectors ( $V$ ) based on the attention scores computed from queries ( $Q$ ) and keys ( $K$ ) [1], [2]. In spiking transformer models [10], [11], this mechanism is adapted to work with spiking neural dynamics ( $SN$ ), typically using Leaky Integrate-and-Fire (LIF) neurons [30] to introduce nonlinearity and improve energy efficiency. Given an input sequence  $X \in \mathbb{R}^{L \times d}$ , with sequence length  $L$  and embedding dimension  $d$ , the  $Q$ ,  $K$ , and  $V$  matrices are obtained via linear projections with learnable weight matrices  $W_Q, W_K, W_V \in \mathbb{R}^{d \times d}$ , followed by spiking neuron activation:

$$Q = SN(XW_Q), \quad K = SN(XW_K), \quad V = SN(XW_V) \quad (1)$$

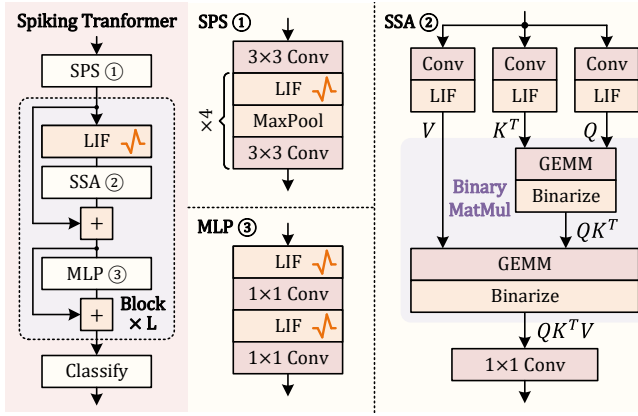


Fig. 2. Overview of typical spiking transformer [17], [18], which begins with a SPS module, followed by  $L$  encoder blocks and a classification head. Each encoder block includes an SSA, an MLP, and associated residual connections.

TABLE I  
BINARY ATTENTION AND RESIDUAL CONNECTION STRATEGIES IN SPIKING TRANSFORMER ARCHITECTURES

Work	Binary Attention	Residual Connection	Network Accuracy	Compute Efficiency
Spikformer [10]	No	Post-Neuron	Low	Low
Spikingformer [11]	No	Pre-Neuron	Medium	Medium
Shen et al. [17]	Yes	Post-Neuron	Medium	Medium
SDT [12] & SDTv2 [13]	Yes	Pre-Neuron	High	High
BESTformer [18]	Yes	Pre-Neuron	High	High

The attention scores are then computed as the dot-product of  $Q$  and  $K$  scaled by  $\sqrt{d}$ . Unlike ViT [4] which applies a softmax function to normalize the scores, spiking attention [10], [11] directly aggregate the result with the value matrix  $V$ :

$$\text{Attention}(Q, K, V) = \text{SN}\left(\frac{QK^T}{\sqrt{d}}V\right) \quad (2)$$

To further enhance efficiency and reduce computational overhead, recent studies have explored binary attention mechanisms [17], [18], which transform both the attention scores  $QK^T$  and the weighted outputs  $QK^TV$  into spiking form. Two prevalent approaches are binarization via spiking neurons and thresholding. The former employs spiking neurons, while the latter emits a spike only if the input current exceeds a learnable threshold  $\Delta$ . This binarization not only reduces computational cost, but also improves network performance, potentially due to the introduced non-linearity [17], [18].

### B. Spiking Transformer Architecture

Spiking transformers extend standard transformer architecture to accommodate processing under SNN paradigm [10], [11]. A typical architecture consists of three main components: a Spiking Patch Splitting (SPS) module, a stack of encoder blocks, and a classification head, as illustrated in Fig. 2.

The SPS module serves as the input interface, employing a series of  $3 \times 3$  spiking convolutional layers with batch normalization to embed spatial information into patch-level representations. These embeddings are then forwarded to

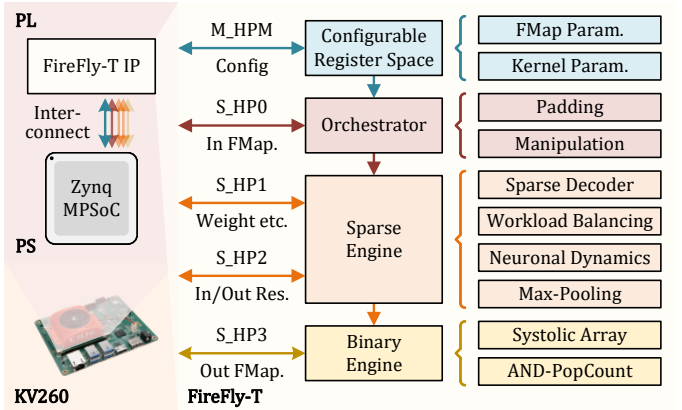


Fig. 3. Block diagram of the FireFly-T system architecture on a Zynq UltraScale+ MPSoC (KV260), highlighting key features and components of FireFly-T IP, alongside the PS-PL interface for control and data transfer.

encoder blocks, each consisting of a Spiking Self-Attention (SSA) module and an MLP. The SSA module comprises the spiking attention mechanism, which performs binary matrix multiplication, and a separate convolutional layer. The MLP is constructed using a series of spiking neurons and  $1 \times 1$  convolutional layers, showcasing the versatility of kernel size selection within spiking transformers.

Residual connections in spiking transformers can be implemented either post-neuron, by adding spikes, or pre-neuron, by adding membrane potentials as illustrated in Fig. 2. We adopt the pre-neuron strategy since it maintains spike-based inputs for all convolutions, preserving computational efficiency, while also allowing residuals to carry richer membrane potential information, which benefits performance [12], [13]. As summarized in Table I, the combination of binary attention and pre-neuron residuals typically enables a spiking transformer architecture that is both high-performing and compute-efficient, making it the preferred choice in this work.

## III. FIREFLY-T BASICS

### A. Overall Architecture

The FireFly-T system is built upon the Processing System (PS) and Programmable Logic (PL) of the Zynq UltraScale+ SoC, as shown in Fig. 3. For command and status control, an M-AXI-HPM master port of the PS side directly interfaces with the FireFly-T IP. To facilitate high-throughput data transfer between the PS and PL, four 128-bit S-AXI-HP ports are enabled. These ports handle specific tasks: loading weights, biases, and membrane thresholds; fetching feature map inputs; writing feature map outputs; and providing a read-and-write interface for residual input and output data.

Within the FireFly-T IP, the architecture is implemented as an overlay consisting of three main modules: the orchestrator, the sparse engine, and the binary engine. During inference, the feature maps of each network layer are processed in a pipelined manner—first by the orchestrator, then by the sparse engine, and finally by the binary engine if attention is enabled. This processing sequence is applied uniformly across all layers, reusing the same hardware throughout inference.

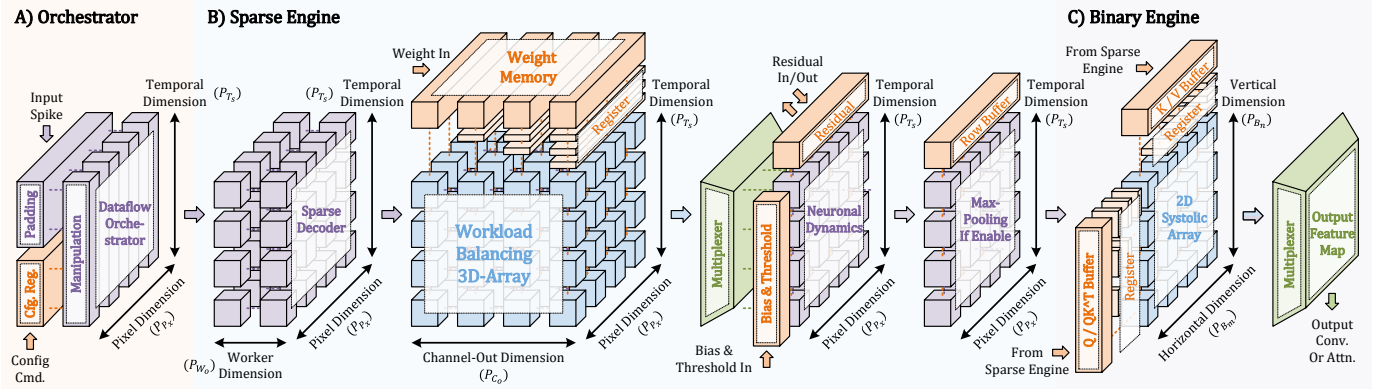


Fig. 4. Illustration of FireFly-T’s parallelism and dataflow, featuring the orchestrator, sparse engine, and binary engine.

**Orchestrator.** The orchestrator acts as the central control unit, obtaining layer-specific configurations—such as feature map and kernel parameters—by accessing a register space configured by the PS side. These configurations are propagated downstream alongside the output data stream to the sparse engine, and subsequently to the binary engine. In addition, the orchestrator also manages padding and performs dataflow manipulation to prepare inputs for the sparse engine. The input and output data formats span multiple dimensions (e.g., pixel, spatial, channel), allowing the computation engine to effectively exploit multi-dimensional parallelism.

**Sparse Engine.** The sparse engine accelerates convolutional and linear operations by exploiting fine-grained activation sparsity. It employs high-throughput multi-lane decoders alongside a scalable, workload-balanced 3D array architecture. The decoder concurrently extracts multiple non-zero indices from vectorized input spikes, leveraging the orchestrator’s throughput and reusing indices across output channels for efficiency. These indices guide computation within the workload-balanced array, which supports scalable spatial, temporal, and channel-in/out parallelism by decoupling load balancing from memory banking. Additionally, pipelined accumulation across output channels enables sequential, group-wise membrane updates, thereby allowing a more compact and resource-efficient neuronal dynamics module. The resulting outputs are passed through a max-pooling module and, if attention is enabled, forwarded to the binary engine for further processing.

**Binary Engine.** The binary engine employs a resource-efficient 2D systolic array to accelerate binary attention operations, notably the  $QK^T$  and  $QK^TV$  computations. It leverages the byte-write capability of SRAMs to implicitly perform dataflow permutations required by spiking attention, eliminating the need for dedicated transposition buffers. At its computational core is the AND-PopCount operation, which is finely optimized to match the granularity of LUT6 resources—enhancing both hardware efficiency and timing closure. Moreover, the binary engine interfaces directly with the sparse engine, consuming intermediate results and operating in a pipelined manner. This close integration reduces off-chip memory traffic and effectively hides the latency of multi-head attention computations which will be detailed in Section III-C.

TABLE II  
NOTATIONS IN FIREFLY-T

Type	Symbol	Description
	$T_s$	Number of time steps
Network Parameter	$K_h, K_w$	Height and width of the kernel
	$C_i, C_o$	Number of input and output channels
	$F_h, F_w$	Height and width of input feature map
Hardware Parallelism	$P_{F_x}, P_{T_s}$	Spatial and temporal parallelism
	$P_{C_i}, P_{C_o}$	Input and output channel parallelism
Hardware Configuration	$M$	Number of sparse decoder lanes
	$P_{W_o}$	Number of load balancing workers

### B. Parallelism and Dataflow

Parallelism in SNNs can typically be exploited along four primary dimensions: temporal, spatial (or pixel-wise), input channels, and output channels. FireFly-T is designed to support parallelism across all four dimensions. For clarity, the notation used throughout this work is summarized in Table II. The input feature map is viewed as  $(T_s, F_h, F_w, C_i)$ , where  $T_s$  denotes the number of time steps,  $F_h$  and  $F_w$  represent the spatial dimensions, and  $C_i$  is the number of input channels. The kernel is defined with dimensions  $(C_o, K_h, K_w, C_i)$ , where  $C_o$  is the number of output channels, and  $K_h, K_w$  specify the kernel’s spatial dimension.

FireFly-T’s parallelism strategy can be characterized by  $(P_{T_s}, P_{F_x}, P_{C_i}, P_{C_o})$ , representing temporal, spatial, input channel, and output channel parallelism, respectively. As depicted in Fig. 4A, the orchestrator comprises  $P_{T_s}$  memory banks, and adopts a unified data format of  $(P_{T_s}, P_{F_x}, P_{C_i})$  for both inputs and outputs, ensuring matched throughput.

The output is subsequently routed to a grid of sparse decoders, organized with dimensions  $(P_{W_o}, P_{T_s}, P_{F_x})$ , as shown in Fig. 4B. Here,  $P_{W_o}$  denotes the worker dimension, which will be elaborated in Section IV-A1. Each decoder is capable of consuming a  $P_{C_i}$ -length spike vector per cycle, and its output indices are reused across the  $P_{C_o}$  dimension. At the core of sparse engine lies a workload balancing 3D array structured as  $(P_{T_s}, P_{F_x}, P_{C_o})$ , where each unit is supported by  $P_{W_o}$  PEs to ensure load distribution. Along the  $P_{C_o}$  dimension, there

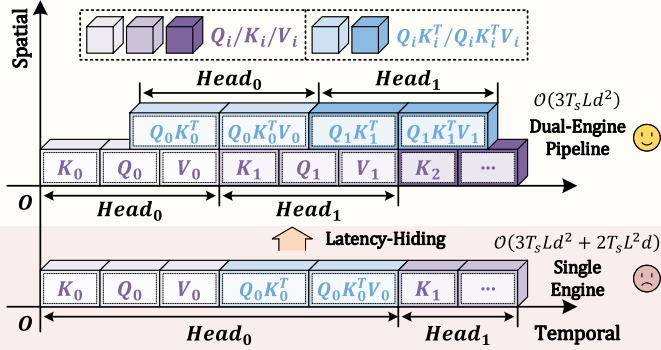


Fig. 5. Spatial-temporal diagram of the latency-hiding pipeline showing overlapped spiking attention execution in the sparse and binary engine.

are  $P_{C_o}$  weight RAMs, each storing  $(K_h \times K_w \times C_i / P_{C_i})$  vectors of  $P_{C_i}$  weights. As described in Section III-A, outputs along the  $P_{C_o}$  dimension are pipelined, reducing the neuronal dynamics module to a  $P_{F_x} \times P_{T_s}$  grid. The output then passes through a max-pooling module, and the dataflow is implicitly manipulated by the binary engine for spiking attention.

The binary engine is organized as a  $(P_{B_m} \times P_{B_n})$  systolic array, as illustrated in Fig. 4C. Upon receiving intermediate results from the sparse engine, each PE in the binary engine performs an AND-PopCount operation on two input vectors, each of length  $P_{B_k}$ . At the output stage, the resulting feature map—whether produced by the sparse or binary engine—is reformatted to align with the input layout  $(P_{T_s}, P_{F_x}, P_{C_i})$  required by the overlay architecture.

### C. Latency-Hiding Pipeline

Fig. 5 illustrates the proposed latency-hiding pipeline, which overlaps spiking attention by having the sparse engine compute  $Q$ ,  $K$ , and  $V$ , while the binary engine simultaneously calculates  $QK^T$  and  $QK^T V$ . Specifically, the binary engine begins computing  $QK^T$  as soon as  $Q$  and  $K$  are available from the sparse engine, overlapping with the sparse engine's calculation of  $V$ . Subsequently, it computes  $QK^T V$ , overlapping with the sparse engine's calculation of next head's  $K$  and part of  $Q$ . This pipelined approach continues across heads, effectively hiding the latency of attention operations ( $QK^T$ ,  $QK^T V$ ) behind linear projections ( $Q$ ,  $K$ ,  $V$ ). As a result, the execution time complexity is reduced from  $\mathcal{O}(3T_s Ld^2 + 2T_s L^2 d)$  to  $\mathcal{O}(3T_s Ld^2)$ , where  $L = F_h \times F_w$  is the sequence length and  $d$  is the embedding dimension.

To implement effective pipelining, the size of the binary engine  $P_{B_m} \times P_{B_n}$  with inner-product parallelism  $P_{B_k}$  should be carefully considered. Assuming the output channel dimension per head is  $P_{C_o}$  for simplicity, we define the computational workloads ( $W_s, W_b$ ) per attention head and the available parallelism ( $P_s, P_b$ ) for the sparse and binary engine as follows:

$$\begin{aligned} W_s &= T_s \times F_h \times F_w \times C_i \times P_{C_o} \\ W_b &= T_s \times F_h \times F_w \times F_h \times F_w \times P_{C_o} \\ P_s &= P_{T_s} \times P_{F_x} \times P_{C_i} \times P_{C_o} \\ P_b &= P_{B_m} \times P_{B_n} \times P_{B_k} \end{aligned} \quad (3)$$

Since three sparse engine operations ( $Q, K, V$ ) overlap with two binary engine operations ( $QK^T, QK^T V$ ), the condition for efficient pipelining is  $3 \times (W_s / P_s) \approx 2 \times (W_b / P_b)$ . Substituting the workload and parallelism definitions from Eq. 3 yields the required relationship between the parallelisms:

$$P_b \approx 2/3 \times (F_h \times F_w / C_i) \times P_s \quad (4)$$

Notably, in typical configurations of spiking transformers evaluated on datasets such as CIFAR-10 and ImageNet [11], [17],  $P_b$  is considerably smaller than  $P_s$ , ranging from one-fourth to one-eighth of  $P_s$ . Furthermore, employing a 4-lane accumulation in the binary engine requires only  $P_{B_m} \times P_{B_n} / 4$  DSP48E2 units, which highlights that the binary engine can support binary attention with latency hiding, while consuming significantly fewer hardware resources than the sparse engine.

## IV. FIREFLY-T MICROARCHITECTURE

### A. High-Throughput Sparse Engine

As outlined in Section III-A, the sparse engine is designed to efficiently exploit the fine-grained sparsity of spiking activations. This is achieved through a multi-lane sparse decoder that supports high-throughput processing of vectorized inputs. In addition, a scalable workload balancing mechanism is introduced, which evenly distributes workloads while avoiding bank conflicts induced by crossbar methods. This approach enables efficient scaling of parallelism across both spatial and temporal dimensions, laying the foundation for the system's multidimensional parallel processing capabilities.

1) **Multi-Lane Sparse Decoder:** We identified a performance bottleneck in existing sparsity-oriented SNN accelerators due to their limited ability to exploit input throughput, which typically corresponds to channel-in parallelism. This stems from the conventional sparse decoder designs: bitmap-based decoders produce only one output (a one-hot vector or index) per cycle, and CSR-based decoding requires serial traversal of column indices [25], [32], [33]. As illustrated in Fig. 6A, with 16-bit input bandwidth, decoding the bitmap input 0x9042 on a single-lane decoder takes four cycles, resulting in an effective throughput of just 1/4, and thus underutilizing the available channel-in parallelism.

To address this limitation, we present a multi-lane sparse decoder with  $M$  lanes, capable of identifying multiple non-zero spike indices in parallel. As depicted in Fig. 6A, a 4-lane decoder ( $M = 4$ ) can process the input bitmap 0x9042 in a single cycle by simultaneously extracting four active spikes, thereby improving throughput. To achieve this, our design draws inspiration from the look-ahead carry generators, where each bit position uses propagate ( $p$ ) and generate ( $g$ ) signals to compute the  $(n+1)$ -th carry-out  $c_{n+1}$  as  $c_{n+1} = g_n \vee (p_n \wedge c_n)$ . We adapt this principle to the architecture of our  $M$ -lane sparse decoder. Specifically, given a sparse input  $i$ , the  $m$ -th lane of the one-hot output  $o$  is computed as follows:

$$\begin{aligned} o_n^m &= (i_n \wedge c_n^{m-1}) \wedge \neg c_n^m \\ &= g_n^m \wedge \neg c_n^m \\ c_{n+1}^m &= (i_n \wedge c_n^{m-1}) \vee c_n^m \\ &= g_n^m \vee (p_n^m \wedge c_n^m) \end{aligned} \quad (5)$$

where  $g_n^m = i_n \wedge c_n^{m-1}$ ,  $p_n^m = c_n^{m-1} = 1$  and  $c_0^m = 0$

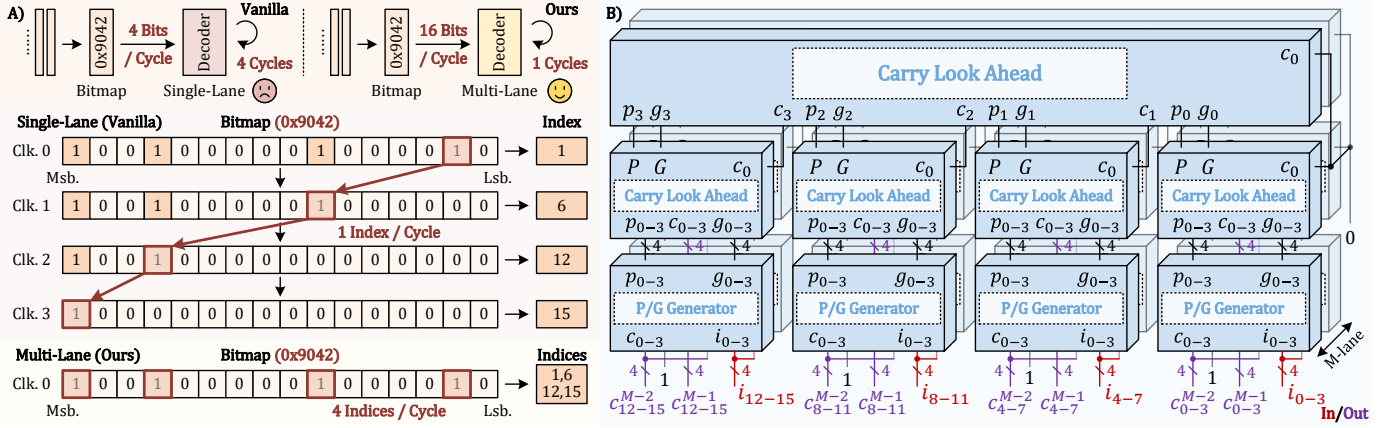


Fig. 6. Bitmap-based sparse decoder. A1) Throughput comparison between single-lane decoder [25], [31] and multi-lane ( $M = 4$ ) decoder, using example inputs 0x9042. A cycle-level decoding process is shown for both single-lane and multi-lane ( $M = 4$ ) decoder. B) Architecture of a multi-lane ( $M = 2$ ) sparse decoder, detailing its intra- and inter-block grouped carry generator organization.

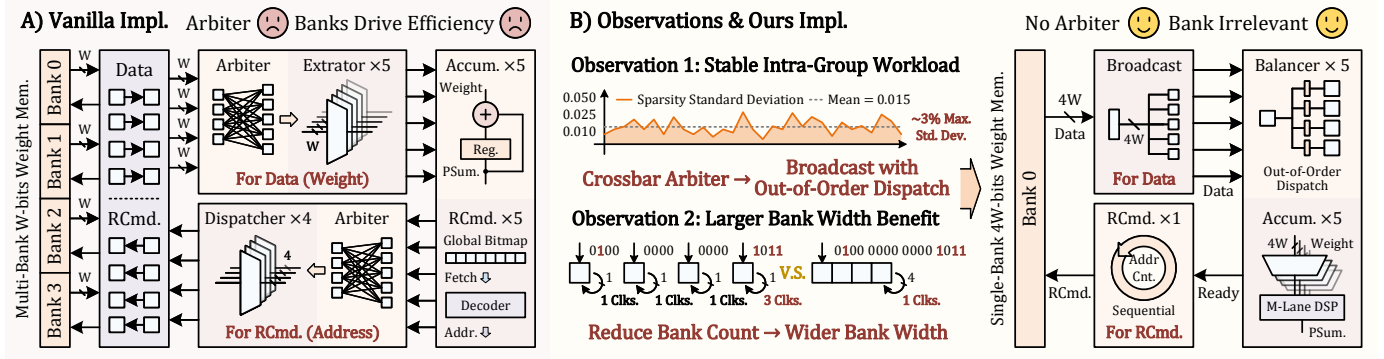


Fig. 7. Workload balancing approaches. A) Vanilla crossbar-based method [22] with four  $W$ -bit weight memory banks. B) Our proposed method motivated by the observations, with a single  $4W$ -bit weight memory bank. Both are demonstrated with the configuration  $P_{C_o} = 1$ ,  $P_{T_s} \times P_{F_x} = 5$  and  $P_{W_o} = 4$ .

Here,  $p_n^m$  is always set, and  $g_n^m$  indicates that the  $n$ -th input bit and the carry-in from lane ( $m - 1$ ) are both active, where  $c_n^{m-1}$  signifies that the  $m - 1$ -th spike has been found prior to position  $n$ . The output  $o_n^m$  is activated if  $g_n^m$  is set—meaning the  $n$ -th input bit is a candidate for the  $m$ -th spike—and no preceding bit has already triggered the current lane ( $\neg c_n^m$ ).

To ensure correct operation across cycles, the input bitmap is updated as  $i_n = i_n \wedge c_{n+1}^{M-1}$ , which clears bits that have already been processed. Meanwhile, an input tracker—initialized by a pop-count of the original input and decremented by a throughput of  $M$  per cycle—controls new input loading, permitting it when its value is less than or equal to  $M$ .

Additionally, the decoder utilizes a grouped structure that enables both intra-block and inter-block parallelism, as illustrated in Fig. 6B, to improve scalability and reduce logic depth for wide inputs. By integrating these features, our sparse decoder achieves high-throughput and effective channel-in parallelism with an efficient hardware implementation.

2) **Scalable Load Balancing:** As discussed in Section I, existing SNN sparse accelerators either lack support for multidimensional parallelism [23], [34], or rely on crossbar-based workload balancing [22], [32]. However, such crossbar-based interconnect typically suffer from performance degradation when scaling parallelism due to increased bank conflicts.

Fig. 7A shows a crossbar-based workload balancing approach employing a banked memory architecture with an all-to-all interconnect [22]. In this design, kernel weights' input channels are partitioned into  $W$ -bit chunks and distributed across four memory banks. An initial arbiter is required to manage concurrent data dispatch from these banks to PEs. Upon receiving a data chunk, the extractor within each PE selects the valid weights based on the non-zero spikes identified by the sparse decoder for membrane potential accumulation.

Subsequently, for fetching further valid weights, each PE decodes its global bitmap to locate the address of the next relevant chunk and issues read commands. A second arbiter then resolves potential access conflicts among these commands before they are dispatched to the memory banks. This dual-arbiter structure introduces additional logic overhead and degrades performance due to increased latency from access conflicts resolution, particularly when the number of PEs does not match the number of banks. For instance, with five PEs and four banks, at least one PE will inevitably stall—unless it accesses the same address and the same bank as another PE.

To set the stage for our proposed architecture, we first discuss two key observations that informed our approach:

**Observation 1.** The sparsity within a kernel window of size  $K_h \times K_w \times C_i$  remains relatively stable across the  $P_{T_s} \times P_{F_x}$

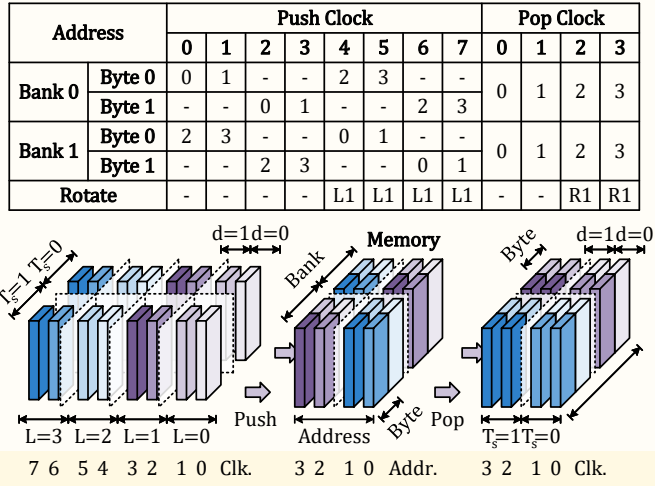


Fig. 8. Cycle-level illustration of implicit dataflow manipulation transforming the data layout from  $(L, d, T_s)$  to  $(T_s, d, L)$ , with  $L = 4$  and  $d = T_s = 2$ . L1 and R1 indicate one-bank left and right rotations across SRAM banks.

dimensions, as empirically demonstrated in Fig. 7B, where the results show that the observed standard deviation is approximately 3% of the theoretical maximum. This is intuitively plausible given the typically large kernel size—particularly in transformer-based architectures—and the inherent spatial-temporal locality of the  $P_{T_s} \times P_{F_x}$  input space.

**Observation 2.** Processing larger vectorized inputs tends to offer higher performance compared to handling multiple smaller vectors. As depicted in Fig. 7B, consider four PEs, each with a sparse decoder throughput of 1, receiving input vectors of 0x4, 0x0, 0x0, and 0xB, respectively. In this configuration, the last PE would require three cycles to complete its task. By contrast, a single PE with a decoder throughput of 4 can process the combined input 0x400B in just one cycle, demonstrating enhanced computational throughput.

Leveraging these observations, we propose a unified memory architecture. As shown in the right part of Fig. 7B, the architecture features a single memory bank that directly broadcasts wider vectorized data across the  $P_{T_s} \times P_{F_x}$  dimension. To scale parallelism along the output channel dimension ( $P_{C_o}$ ), the architecture is instantiated per channel, while the indices from sparse decoders are reused. This leads to a 3D processing array organized as  $(P_{C_o}, P_{T_s}, P_{F_x})$ . In this array, we incorporate an additional worker dimension,  $P_{W_o}$ , enabling out-of-order dispatch of computations across the  $K_h \times K_w \times C_i$  dimensions to idle workers, improving workload balance. Each worker is responsible for extracting valid weight data corresponding to  $M$  non-zero indices—provided by the  $M$ -lane sparse decoder—for membrane potential accumulation.

This design directly leverages **Observation 1**: stable intra-group sparsity ensures the efficiency of broadcasting a large, vectorized data chunk from the unified, wide memory bank, as most PEs can retrieve their required weights within the broadcast. The wide-bank structure also aligns with the wider vector operations discussed in **Observation 2**. Integrated with our multi-lane sparse decoders, this enables efficient extraction of multiple weights from the wide vector, enhancing com-

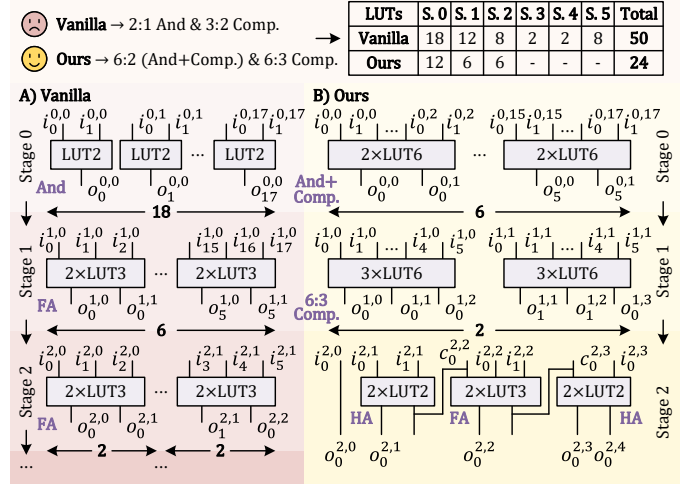


Fig. 9. Comparison between the vanilla AND-PopCount [24] and our LUT6-optimized approach with two 18-bit input vectors. Here,  $i_k^{m,n}$  denotes the  $n$ -th bit of the  $k$ -th input at stage  $m$ , propagated from output  $o_k^{m-1,n}$ .

putational throughput. Unlike crossbar-based designs—which require more memory banks to scale with spatial-temporal parallelism—our approach eliminates the need for arbiters and multi-banks, achieving more stable performance scaling under fixed vector lengths, as detailed in Section V-C.

### B. Resource-Efficient Binary Engine

As described in Section III-A, the binary engine is designed to support efficient binary attention computation by incorporating latency hiding while maintaining minimal resource overhead. In this section, we delve into the key techniques that underpin its resource efficiency, including implicit dataflow manipulation and LUT6-optimized AND-PopCount logic.

**1) Implicit Dataflow Manipulation:** Consider matrices  $Q$ ,  $K$ , and  $V$  at a specific timestep, each of size  $L \times d$ , where  $L$  is the sequence length and  $d$  is the embedding dimension. When computing  $QK^T$ , assuming  $Q$  and  $K$  are stored in row-major order, the inner products are computed row-by-row, producing an  $L \times L$  attention score. However, when multiplying it with  $V$ , the inner products are computed row-by-column. Hence, to ensure consistent row-wise memory access and reuse reading logic,  $V$  must be transposed to have dimensions  $d \times L$ .

Since attention mechanism involves transposing within  $QK^T V$  computation, and given the necessity to permute the temporal dimension into an outer dimension to avoid instantiating the 2D systolic array  $T_s$  times in the binary engine, we propose an implicit dataflow manipulation technique that treats the SRAM as a three-dimensional structure—(bank, address, byte)—and leverages its byte-write granularity to perform in-place data manipulation during push operations, thereby avoiding the need for an explicit buffer.

Fig. 8 presents a cycle-level example of the proposed implicit dataflow manipulation on the value matrix  $V$ , reordering the data layout from  $(L, d, T_s)$  to  $(T_s, d, L)$ . During the push phase, data is written into  $T_s$  banked RAMs using interleaved addressing with a stride of  $d$ . In the pop phase, consistent addressing across banks allows the permutation between the  $d$

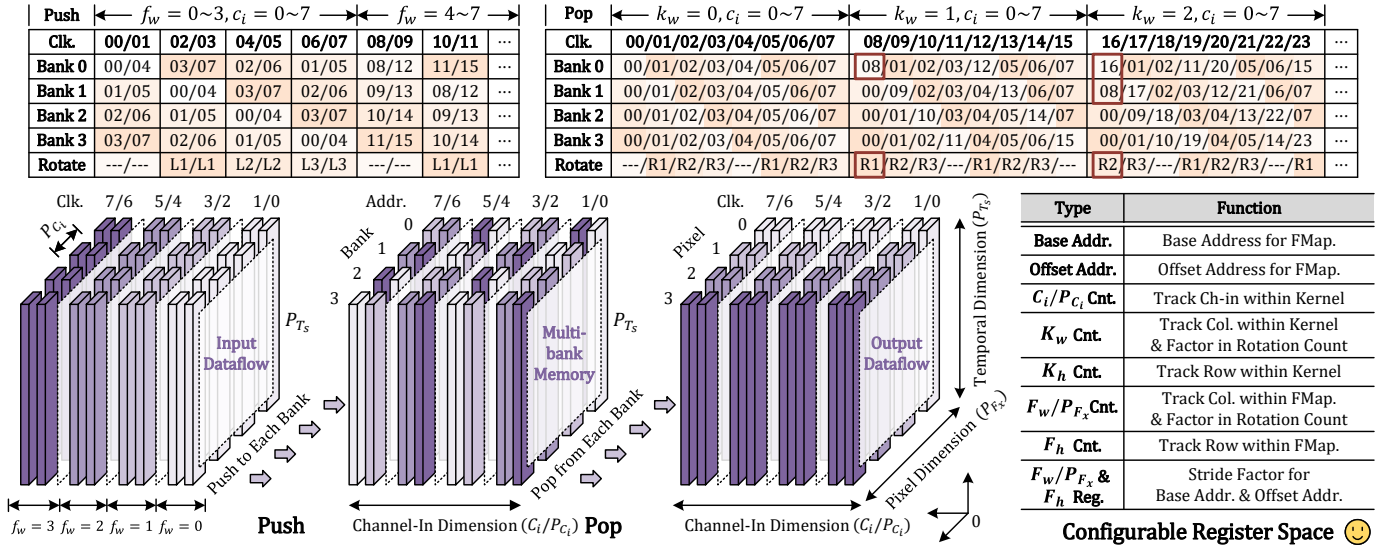


Fig. 10. Cycle-level illustration of the orchestrator’s push and pop phases, demonstrating the interleaved addressing mechanism for data layout transformation. The example uses  $F_w = C_i = 8$ ,  $K_h = K_w = 3$ , and  $P_{F_x} = 4$ . Parameters such as  $C_o$ ,  $F_h$ ,  $P_{T_s}$ , and  $P_{C_i}$  are omitted here for simplicity.

and  $T_s$  dimensions. Within each bank,  $L \times d$  data is streamed in, with push addresses incrementing cyclically along the  $d$  dimension and the byte-write mask cyclically rotates along the  $L$  dimension, thereby introducing an additional permutation across the  $d$  and  $L$  dimensions. To fully cover the interleaved address space, both push addresses and input data are rotated across banks every  $L$  push cycles. This rotation is reversed during the pop phase to preserve alignment and ensure the correct transposed layout is reconstructed.

Through this overall process, the 3D matrix layout is implicitly manipulated without the need for additional buffering. Such an approach not only minimizes hardware overhead but also enables flexible alignment of the sparse engine’s output throughput with the binary engine’s input bandwidth, supporting the requirements of the latency-hiding pipeline.

2) **LUT6-Optimized AND-PopCount Logic:** In binary attention mechanisms, the inner product computation within the PEs of systolic array reduces to a bitwise AND followed by a population count. As this forms a fundamental computation, optimizing the AND-PopCount operation is crucial for improving the resource efficiency of the binary engine.

Xilinx FPGAs are built around LUT6 logic units, each capable of implementing arbitrary boolean functions with up to six inputs and one output. However, the straightforward implementation of the AND-PopCount as used by Gao et al. [24] does not fully utilize the capacity of these LUT6s. As shown in Fig. 9A, AND gates typically require only two inputs, and directly implementing the popcount logic by Full Adders (FAs, or 3:2 compressors) and Half Adders (HAs) also fails to exploit the full six-input granularity of the LUT6. As a result, such designs lead to inefficient resource utilization and increased logic depth, which worsens timing performance.

To address these inefficiencies, we propose an optimized AND-PopCount implementation that configures LUT6s as specialized compressors. As illustrated in Fig. 9B, in the initial stage, two LUT6 functions as a 6:2 compressor, performing

both the bitwise AND operations and an initial population count simultaneously. Subsequent stages employ efficient 6:3 compressors, constructed from three LUT6s, to further reduce the intermediate sums. The final two operands are then processed using a carry-propagating adder composed of FAs and HAs, yielding the final population count.

This multi-stage reduction architecture [35] with dedicated compressors takes full advantage of the six-input granularity of LUT6s. Compared to the naive approach [24], it significantly reduces both logic depth and LUT6 consumption. For example, in Fig. 9 with the case of two 18-bit inputs, our method reduces logic depth from 5 to 2 stages and achieves a 52% reduction in LUT6 usage, thereby improving timing closure and enhancing the overall efficiency of the binary engine.

### C. Flexible Orchestrator

The orchestrator, introduced in Section III-A, receives the current layer configuration from the PS and propagates it downstream—first to the sparse engine, followed by the binary engine. Additionally, it transforms the input layout for the sparse engine, which supports flexible kernel configurations and a data layout derived from tiling along multiple parallel dimensions. This transformation will be elaborated below.

1) **Input Dataflow Orchestration:** According to the parallelism and dataflow outlined in Section III-B, the orchestrator’s input dataflow is structured as  $(C_o/P_{C_o}, T_s \times F_h \times F_w \times C_i/(P_{T_s} \times P_{F_x} \times P_{C_i}), P_{T_s} \times P_{F_x} \times P_{C_i})$ , while the output dataflow is defined as  $(C_o/P_{C_o}, T_s \times F_h \times F_w \times K_h \times K_w \times C_i/(P_{T_s} \times P_{F_x} \times P_{C_i}), P_{T_s} \times P_{F_x} \times P_{C_i})$ . In our design,  $P_{F_x}$  performs tiling along  $C_i$  dimension for the input and along the spatial dimension for the output, since tiling by channels improves padding efficiency by replacing per-pixel operations with a single padding step per vectorized channel slice.

To support the required dataflow transformation, as illustrated in the push phase of Fig. 10, we employ a banked memory architecture consisting of  $P_{F_x}$  memory banks. Each

bank features a bit width of  $P_{T_s} \times P_{C_i}$ , and is pushed to using an interleaved push-addressing mechanism. Initially, the push addresses across the banks are offset by a stride of 1, and incremented by a stride of  $P_{F_x}$ , allowing  $P_{F_x}$  channel slices to be written to sequential addresses. After each full iteration over  $C_i/(P_{F_x} \times P_{C_i})$  channel slices, the push address pointer resets, and a cyclic bank-shifting mechanism rotates both the address pointers and the data slices across the banks. This results in an interleaved layout where channel slices of different spatial grid are stored with rotated bank mappings.

Therefore, during the pop phase—when all banks access the same address in each cycle with address increments continuously, and the fetched data slices are reverse-rotated to undo the earlier push-time shift—the layout associated with  $P_{F_x}$  transitions from a channel-wise format to spatial tiling, naturally aligning with the target output data organization.

2) **Output Dataflow Orchestration:** The output dataflow requires structured iteration over the dimensions, starting with  $C_i/P_{C_i}$ , followed by  $K_h \times K_w$ . The same pop mechanism described in Section IV-C1 is employed to retrieve the first channel-in block for the kernel window. Fig. 10 illustrates this behavior at the cycle level during its pop phase, specifically for the case where  $k_w = 0$  and  $c_i = 0 \sim 7$ .

To progress through the  $K_h \times K_w$  dimension, the memory addressing mechanism must adapt to the kernel window’s horizontal sliding. As illustrated in the pop phase of Fig. 10, after each full iteration over  $C_i/P_{C_i}$  for a given  $k_w$ , most bank address pointer reset to their initial state ( $c_i = 0$ , stored in the base address register). Exceptions are the first  $k_w$  banks; their addresses are updated by circularly incrementing from the preceding bank’s address (with wrap-around), fetching the new data column necessitated by the kernel’s shift. The rotation counter also resets to  $k_w$ , instead of its initial state, to preserve spatial alignment. By extending this control principle to the remaining outer loops, the system flexibly orchestrates the target output dataflow without any performance stalls.

Unlike Fang et al.’s overlay architecture [25] with its fixed  $3 \times 3$  compute grid tailored for  $3 \times 3$  kernel operations—resulting in resource underutilization for other kernel sizes such as  $1 \times 1$ —our orchestrator flexibly supports arbitrary kernel configurations without compromising throughput or resource efficiency. This adaptability stems from a lightweight, configurable register space as shown in Fig. 10. Managed by the PS side of Zynq SoC, these registers define control parameters (e.g., stride, rotation, layer-specific settings) to direct the dedicated push/pop control logic, while also propagating metadata—such as accumulation loop counts and attention enable flags—to the downstream sparse and binary engines.

## V. EXPERIMENTS

### A. Experiments Setup

To evaluate FireFly-T’s performance, we conduct a series of experiments with various SNN models, including CIFAR-Net (as evaluated in FireFly v2 [27]) and two spiking transformer setups: Spikingformer-4-256 and Spikingformer-8-512, where the numerals denote the number of encoder blocks and embedding dimension, respectively. CIFAR-Net and Spikingformer-

4-256 are evaluated on CIFAR-10, whereas Spikingformer-8-512 is assessed on ImageNet. All models are trained using the BrainCog framework [36] and quantized to 4-bit precision following the method proposed in FireFly-S [31].

Hardware deployment and validation are performed on the Xilinx Zynq UltraScale+ FPGA, using the edge-oriented KV260 Vision AI Starter Kit. FireFly-T is developed in SpinalHDL, with Verilog generated via its compiler. These Verilog files are synthesized and implemented through the Xilinx Vivado 2024.2. Power consumption estimates are then obtained from the Vivado’s implementation reports.

### B. Sparse Decoder Configuration

Fig. 11 presents a layer-wise sparsity analysis for CIFAR-Net, Spikingformer-4-256 and Spikingformer-8-512. The findings reveal that the spiking transformers exhibit regular sparsity patterns across the encoder blocks, and all SNN models demonstrate a high and relatively stable sparsity (exceeding 75%) without requiring additional optimization techniques.

For general analysis, we implement a simulator configured under 75% spike sparsity. Within this framework, the initial optimization focuses on the configuration of  $P_{C_i}$ , the input bit-width of the sparse decoder, subject to a fixed throughput  $G = P_{W_o} \times M$ , which indicates the maximum processing capacity per grid point in the 3D workload balancer to extract valid weights for non-zero activations each cycle.

Following the aforementioned configuration, we define performance  $R = 1/D$ , where  $D$  is the overall simulated processing latency. To evaluate the performance-resource trade-off, resource efficiency is given by  $\eta = R/B$ , with  $B = \lambda \times P_{C_i}$  denoting resource utilization and  $\lambda$  being a constant scaling factor. Our primary goal is to maximize performance  $R$  without overly compromising resource efficiency  $\eta$ . To capture this balance, a composite performance metric  $F$  is defined as:

$$F = \eta R = \frac{1}{\lambda \times P_{C_i} \times D^2} \quad (6)$$

The simulation results, presented in Fig. 12, first reveal that for a given throughput  $G$ , the optimal input bit-width  $P_{C_i}$  that maximizes the composite performance metric  $F$  aligns closely with workload characteristics dictated by spike sparsity. For instance, at  $G = 4$ , a  $P_{C_i}$  value of  $G/(1-0.75) = 16$  is near-optimal for maximizing  $F$ . This phenomenon is intuitive: for a fixed  $G$ , exceeding this optimal  $P_{C_i}$  offers no additional throughput gains as PEs become saturated, whereas a  $P_{C_i}$  below the optimum leads to PE underutilization, making input bandwidth the bottleneck. Crucially, analysis of the maximum  $F$  achieved with these optimal  $P_{C_i}$  settings (the final subplot of Fig. 12) further reveals a clear linear scaling with  $P_{C_i}$ . This demonstrates the system architecture’s **scalability of channel-in parallelism** without performance saturation.

Subsequently, the impact of the number of decoder lanes  $M$  on performance  $R$  is evaluated at fixed throughput  $G$ , using the aforementioned optimal  $P_{C_i}$  (16 for  $G = 4$  and 32 for  $G = 8$ ). As shown in Fig. 13A, increasing  $P_{W_o}$  (indicating reducing  $M$ ) enhances  $R$  via improved load balancing with more workers. While these gains exhibit diminishing returns and introduce resource overhead, we observe that a

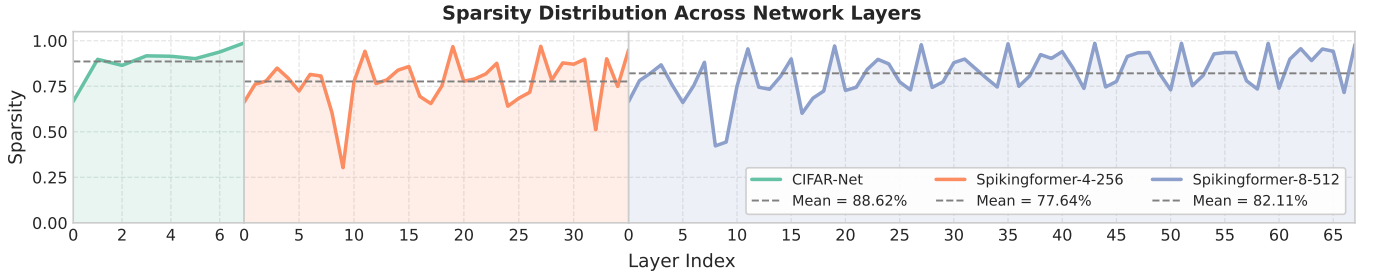


Fig. 11. Layer-wise sparsity distribution in CIFAR-Net, Spikingformer-4-256, and Spikingformer-8-512.

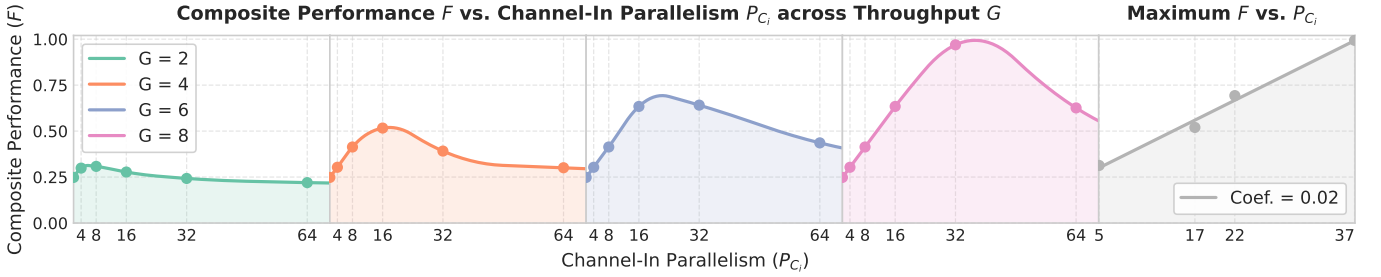


Fig. 12. Simulation results illustrating the relationship between normalized composite performance ( $F$ ) and channel-in parallelism ( $P_{C_i}$ ) across various throughput ( $G$ ). Left:  $F$  versus  $P_{C_i}$  for several throughput values ( $G$ ), assuming 75% sparsity. Right: Maximum achieved  $F$  across different  $P_{C_i}$ .

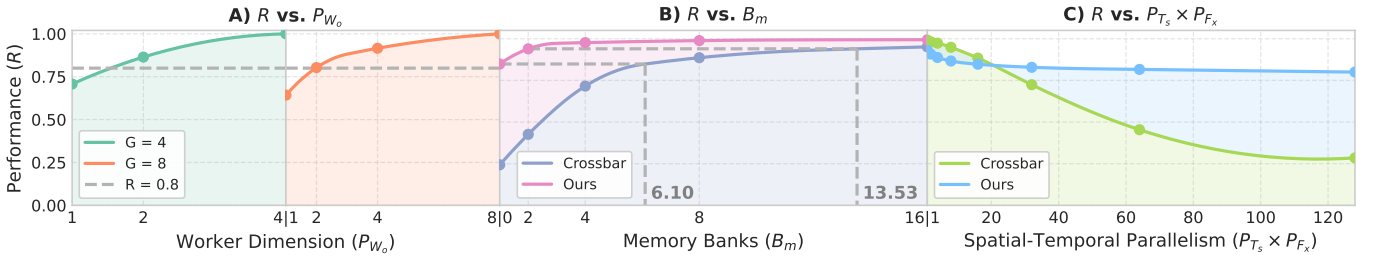


Fig. 13. Performance analysis across different configurations. A) Relationship between performance  $R$  and worker dimension  $P_{W_o}$ , where  $P_{C_i} = 16$  for  $G = 4$  and  $P_{C_i} = 32$  for  $G = 8$ . B) Impact of memory bank  $B_m$  on performance  $R$  with  $P_{C_i} = P_{T_s} \times P_{F_x} = 16$ . C) Scalability comparison between our method ( $B_m = 1$ ) and the crossbar-based approach [22] ( $B_m = 8$ ) as  $P_{T_s} \times P_{F_x}$  increases, with  $P_{C_i} = 16$ .

configuration of  $P_{W_o} = 2$  (implying  $M = 2$  for  $G = 4$  and  $M = 4$  for  $G = 8$ ) notably achieves over 80% of the peak performance. This result highlights that our architecture can deliver substantial performance through multi-lane sparse decoder even with a reduced worker dimension, achieving a favorable balance between throughput and resource efficiency.

### C. Load Balancing Evaluation

To evaluate our proposed workload balancing mechanism and assess the impact of bank conflicts inherent in crossbar-based method [22], [32], simulation are conducted with a configuration of  $P_{C_i} = P_{T_s} \times P_{F_x} = 16$ . Notably, our approach utilizes a single-bank design. Therefore, for a fair comparison with consistent total memory bandwidth, the throughput width of our single bank is proportionally scaled as the number of banks in the crossbar method increases.

As presented in Fig. 13B, our approach offers clear advantages. The crossbar-based method's performance substantially deteriorates with insufficient memory banks, primarily due to

conflicts caused by data reuse inherent in spatial-temporal parallelism. In contrast, our method exhibits more stable and superior performance. Specifically, with  $B_m = 1$  and comparable resource consumption, our approach achieves a 3.48 $\times$  speedup; conversely, to achieve equivalent performance, the crossbar method would necessitate 6 $\times$  more memory bandwidth, highlighting our effective workload balancing.

We evaluate scalability by comparing our method ( $B_m = 1$ ) with the crossbar-based approach ( $B_m = 8$ , chosen to match our initial performance) as the spatial-temporal parallelism  $P_{T_s} \times P_{F_x}$  increases, while maintaining  $P_{C_i} = 16$ . As shown in Fig. 13C, our method achieves better scalability than the crossbar-based approach. Specifically, when  $P_{T_s} \times P_{F_x}$  increases from 1 to 128, our method experiences only a 13.17% performance loss, whereas the crossbar-based method suffers a substantial 70.68% degradation. These results confirm the enhanced **scalability of spatial-temporal parallelism** by our proposed workload balancing mechanism, laying the foundation for our multidimensional parallelism design.

TABLE III  
PARALLELISM AND SPARSITY SUPPORT OF EXISTING ACCELERATORS

Work	Spatial	Temporal	Ch-Out	Ch-In	Sparsity
TC'23 [28]	Yes	No	Yes	Yes	Not Supported
TCAD'24 [27]	Yes	Yes	Yes	Yes	Not Supported
MICRO'24 [22]	Yes	Yes	No	Yes	Coarse-Grained
JSSC'24 [25]	No	Yes	Yes	Yes	Coarse-Grained
TCAS-I'24 [31]	No	No	Yes	Yes	Fine-Grained
<b>Ours</b>	<b>Yes</b>	<b>Yes</b>	<b>Yes</b>	<b>Yes</b>	<b>Fine-Grained</b>

#### D. Comprehensive Evaluation

**Parallelism and Sparsity Support.** Table III compares recent high-performance SNN accelerators regarding their parallelism and sparsity support. A common challenge is that achieving fine-grained sparsity support often introduces dataflow irregularity, which complicates parallel execution and typically leads to load imbalance. To the best of our knowledge, FireFly-T is the first SNN accelerator designed to exploit fine-grained sparsity while maintaining multidimensional parallelism scalability across spatial-temporal, input-channel, and output-channel dimensions, as experimentally validated in Sections V-B and V-C. This capability is primarily due to the co-designed sparse engine, which integrates a scalable load-balancing 3D array with high-throughput sparse decoders optimized for fine-grained sparsity exploitation.

**Performance and Energy Efficiency.** Based on the previous experimental results, we configure the parallelism of FireFly-T as  $(P_{T_s} \times P_{F_x}, P_{C_i}, P_{C_o}) = (8, 16, 64)$ , aligning with the theoretical peak GOP/s performance of our prior dense accelerator, FireFly v2 [27], on the same hardware platform. The throughput  $G$  is set to 2 for CIFAR-Net and 4 for spiking transformer, respectively. These settings are adopted in the comparative experiments presented in Table IV.

Specifically, E3NE [37] and SyncNN [34] represent early-stage SNN accelerators. E3NE employs an instruction-based end-to-end framework but lacks sparsity exploitation, leading to comparatively low throughput (11.33 GOP/s on MNIST). SyncNN utilizes mixed-precision quantization with a spatial architecture, achieving higher energy efficiency compared to E3NE (3.33 vs. 139.32 GOP/s/W on MNIST), but demands relatively high LUT and DSP consumption.

Recent efforts such as DeepFire2 [28] and FireFly v2 [27] have demonstrated high performance: DeepFire2 achieves notable throughput (1.56kFPS and 21.10 TOP/s on ImageNet), while FireFly v2 delivers higher energy efficiency (633.33 vs. 447.00 GOP/s/W on ImageNet). However, DeepFire2's spatial architecture demands per-layer logic instantiation, incurring substantial resources (1757/960 B/URAMs and 5400 DSPs), and both works lack sparsity support and are limited to spiking convolutional networks, constraining network accuracy. FireFly-T overcomes these limitations, delivering enhanced energy efficiency gains: 13.87 $\times$  and 1.39 $\times$  over DeepFire2 and FireFly v2 on CIFAR10, and 1.75 $\times$  and 1.23 $\times$  on ImageNet, respectively. By exploiting fine-grained sparsity, FireFly-T improves DSP efficiency (GOP/s/DSP) by 4.21 $\times$

over FireFly v2 on CIFAR-Net. Even with the more complex Spikingformer-8-512 architecture (71.55% accuracy), FireFly-T consumes 17.76 $\times$  fewer DSPs and exhibits a 6.21 $\times$  lower GOP/s than DeepFire2's VGG11 baseline (40.10% accuracy), yet still delivers a 2.85 $\times$  improvement in DSP efficiency.

Several prior efforts have targeted transformer acceleration. HeatViT [38] introduced image-adaptive token pruning, achieving 1.25 TOP/s throughput. SSR [39] improves energy efficiency over HeatViT, from 46.82 GOP/s/W to 246.15 GOP/s/W. Despite their notable network performance, both architectures demand substantial hardware resources (1968 DSPs for HeatViT; 1797 DSPs and 394 AIEs for SSR), due to the computationally intensive dense MAC operations, limiting their energy efficiency. SpikeTA [24] supports spiking transformer with DSP-efficient addition trees and depth-aware buffer management, achieving enhanced energy efficiency of 403.99 GOP/s/W. However, its scope is confined to the encoder block, and the spatial architecture without sparsity support limiting deployment to costly U280 device. In comparison, FireFly-T achieves 1.93 $\times$  to 16.68 $\times$  higher energy efficiency and 1.83 $\times$  to 50.50 $\times$  higher DSP efficiency than these transformer-enabled accelerators. Utilizing an overlay architecture, FireFly-T flexibly supports various network topology, while requiring an order of magnitude less resource usage, enabling deployment on resource-constrained edge devices.

**Resource Breakdown.** Table V provides a detailed breakdown of resource utilization within FireFly-T where  $G$  is set to 4. As shown, the binary engine consumes only 11.98% of the LUTs used by the sparse engine, primarily due to its 1-bit operand design—enabled by the spiking attention mechanism—and an optimized implementation of the AND-PopCount logic. Additionally, the binary engine utilizes just 6.10% of the DSP resources compared to the sparse engine, consistent with the analysis in Section III-C. These results highlight the resource efficiency of the binary engine.

Table VI presents the LUT breakdown within the sparse engine, allowing an assessment of resource overhead from fine-grained sparsity support. The sparse decoder, dedicated to input bitmap decoding, utilizes only 5.73% ( $G = 2$ ) and 3.62% ( $G = 4$ ) of the engine's LUTs. This efficiency is a direct result of our input reuse strategy, which permits broadcasting decoded indices across output channels. In contrast, the load-balancing array commands the majority of LUT resources (75.86% for  $G = 2$  and 84.20% for  $G = 4$ ). This is expected, as it forms the engine's core computational logic for workload distribution and valid weight extraction within PEs.

Despite the additional resource overhead, the trade-off turns out to be highly beneficial: enabling sparsity support substantially reduces DSP usage, achieving a fractional reduction of  $1 - G/P_{C_i}$ . Under our parallelism setup, this corresponds to DSP savings of 896 ( $G = 2$ ) and 768 ( $G = 4$ ), compared to 1024 4-lane DSPs required by the dense method. According to the conversion factor from [40] (1 DSP  $\approx$  86 LUTs), these reductions are equivalent to 77k and 66k LUTs, respectively. In contrast, the combined logic overhead from the decoder and load-balancing is significantly lower—18k LUTs ( $G = 2$ ) and 34k LUTs ( $G = 4$ ), highlighting the efficiency and practicality of the proposed design for sparse acceleration.

TABLE IV  
COMPARISON WITH RELATED WORK FOR MULTIPLE IMAGE CLASSIFICATION TASKS.

Work (Type)	Network			Performance				Resource			Deployment	
	Model	Dataset	Acc.	FPS	GOP/s	GOP/s/W	DSP Eff.	kLUTs	B/URAMs	DSPs	Freq.	Device
E3NE [37] (D+C) <sup>1</sup>	LeNet5	MNIST	99.30	3401	11	3.33	-	27	-	-	200	
	AlexNet	CIFAR10	80.60	14	3	0.80	-	48	-	-	150	xcvu13p
	VGG11	CIFAR100	65.00	6	11	2.24	-	88	-	-	150	
SyncNN [34] (S+C)	LeNet-L	MNIST	99.60	1629	55	139.32 <sup>2</sup>	0.10	224	-	554	200	
	NIN	CIFAR10	88.09	147	52	131.93 <sup>2</sup>	-	-	-	-	200	xczu9eg
	VGG13	SVHN	95.65	65	29	74.24 <sup>2</sup>	-	-	-	-	200	
DeepFire2 [28] (D+C)	VGG9	CIFAR10	87.10	23000	543	70.54	0.26	125	511/80	2025	550	
	VGG9	CIFAR100	65.90	11600	10400	518.00	3.60	183	289/452	2881	500	xcvu9p
	VGG11	ImageNet	40.10	1560	21100	447.00	3.90	371	1757/960	5400	450	
FireFly v2 [27] (D+C)	CIFAR-Net <sup>3</sup>	CIFAR10	93.60	334	3443	702.74	6.73	26	87/8	512	250/500 <sup>5</sup>	
	CIFAR-Net <sup>4</sup>	CIFAR100	74.70	222	3625	739.81	7.08	26	87/8	512	250/500 <sup>5</sup>	xczu5ev
	SEW-ResNet34	ImageNet	62.4	40	3103	633.33	6.06	26	87/8	512	250/500 <sup>5</sup>	
HeatViT [38] (S+T)	DeiT-T	ImageNet	72.20	183	440	46.82	0.22	137	355/-	1968	150	
	DeiT-B	ImageNet	80.10	36	12500	110.13	6.05	161	589/-	2066	150	xczu9eg
SSR [39] (D+T)	DeiT-T	ImageNet	72.20	4540	10900	246.15	6.06	620	624/104	1797	230/1000 <sup>6</sup>	
	LV-ViT-T	ImageNet	79.10	2630	8210	181.74	-	-	-	-	230/1000 <sup>6</sup>	xcvc1902
SpikeTA [24] (D+T)	Spikingformer <sup>7</sup>	CIFAR10	95.60	-	28980	408.57	3.99	503	1366/576	7249	450	
	Spikingformer <sup>7</sup>	CIFAR100	78.40	-	28980	405.60	3.99	503	1366/576	7249	450	xcu280
	Spikingformer <sup>8</sup>	ImageNet	74.56	-	28990	403.99	4.04	501	1572/594	7168	450	
FireFly-T (S+C+T)	CIFAR-Net <sup>3</sup>	CIFAR10	93.60	354	3630	978.61	28.35	24	74/0	128	300	
	Spikingformer <sup>9</sup>	CIFAR10	94.45	907	3029	696.64	9.96	46	100/0	304	300	xczu5ev
	Spikingformer <sup>8</sup>	ImageNet	71.55	50	3397	781.13	11.11	46	100/0	304	300	

<sup>1</sup> D: Dense, S: Sparse, C: Convolution, T: Transformer

<sup>2</sup> SyncNN calculates power usage by measuring the active power consumption of the FPGA board (24.5 W) and subtracting the static power measured when the board is idle (24.1 W). Conversely, it is believed that most existing research acquires power metrics directly from the Vivado report.

<sup>3</sup> 3x32x32-32c3-256c3-256c3-mp2-256c3-256c3-256c3-mp2-512c3-mp2-1024c3-ap-10

<sup>4</sup> 3x32x32-64c3-256c3-256c3-mp2-256c3-512c3-512c3-mp2-512c3-mp2-1024c3-ap-10

<sup>5</sup> The base clock frequency of FireFly v2 is 250 MHz, with a DSP double data rate clock of 500 MHz.

<sup>6</sup> SSR is implemented on the AMD ACAP VCK190 board, with PL operating at 230 MHz and the AI Engine (AIE) running at 1 GHz.

<sup>7,8,9</sup> Entries 7, 8, and 9 correspond to Spikingformer-2-512, Spikingformer-8-512, and Spikingformer-4-256, respectively.

TABLE V  
BREAKDOWN OF RESOURCE USAGE FOR FIREFLY-T WITH  $G = 4$ .

Component	kLUTs	kREGs	BRAMs	DSPs
Sparse Engine	40 (34.0%)	109 (46.8%)	72 (50.0%)	288 (23.1%)
Binary Engine	5 (4.1%)	9 (3.7%)	24 (16.7%)	16 (1.3%)
Orchestrator	1 (1.2%)	1 (0.5%)	4 (2.7%)	0 (0.0%)
<b>Total</b>	<b>46 (39.5%)</b>	<b>117 (49.8%)</b>	<b>100 (69.5%)</b>	<b>304 (24.4%)</b>

TABLE VI  
BREAKDOWN OF LUT USAGE FOR FIREFLY-T'S SPARSE ENGINE.

Config	Decoder	Balancer	Neuron	Others
$G = 2$	1306 (5.73%)	17280 (75.86%)	2138 (9.39%)	2055 (9.02%)
$G = 4$	1442 (3.62%)	33536 (84.20%)	2293 (5.76%)	2557 (6.42%)

## VI. RELATED WORK

Recent years have witnessed extensive efforts in designing hardware accelerators for spiking convolutional networks [27],

[28], [31], [40]. FireFly v2 [27] proposes an overlay architecture with spatial-temporal dataflow and double data rate clocking on DSPs [41]. FireFly-S [31] introduces a software-hardware co-design leveraging dual-side sparsity. DeepFire2 [28] presents a spatial architecture employing split-kernel mapping to efficiently scale up SNN processing. Despite these advancements, existing designs either fail to effectively leverage sparsity in overlay architectures or perform poorly on large-scale datasets such as ImageNet, making them unsuitable for adaptation to spiking transformer.

Several accelerators have been proposed for non-spiking transformer models [38], [39], [42]. ViA [42] customizes the hardware design by employing a half-layer mapping strategy tailored for ViT. HeatViT [38] introduces a hardware-efficient, image-adaptive token pruning framework to optimize performance. SSR [39] presents a sequential spatial hybrid architecture that explores the trade-off between latency and throughput. Although these non-spiking transformer accelerators achieve high prediction accuracy, they typically lack energy efficiency and demand high-end hardware resources.

In the emerging field of spiking transformer acceleration, SpikeTA [24] introduces DSP-efficient addition trees and depth-aware buffer management techniques. However, its spatial architecture limits resource reuse and lacks mechanisms for exploiting sparsity. Similarly, Fang et al. [25] propose an overlay architecture based on a fixed  $3 \times 3$  compute grid, which suffers from performance degradation under diverse kernel configurations and fails to leverage fine-grained sparsity to further improve energy efficiency.

## VII. CONCLUSION

FireFly-T marks a substantial advancement over our prior designs, FireFly v2 and FireFly-S, distinguished by its support for spiking transformers, high-throughput fine-grained sparsity exploitation, and multidimensional parallelism, all enabling efficient end-to-end SNN deployment. This is achieved through a dual-engine overlay architecture: the sparse engine employs multi-lane sparse decoder and a bank-conflict-free workload balancer to effectively exploiting sparse inputs, with enhanced scalability for multidimensional parallelism; the binary engine utilizes implicit dataflow manipulation and LUT6-Optimized AND-PopCount logic, enabling resource-efficient spiking attention support. Complementing the dual-engine, an orchestrator flexibly manages dataflow, ensuring adaptability to diverse network topologies for the overlay architecture.

Experimental validation confirmed FireFly-T's superior energy and DSP efficiency across a range of datasets and SNN architectures. Relying on commercial FPGA edge devices, FireFly-T offers a practical and accessible hardware solution. In the future, we will continue to advance SNN hardware that effectively supports the rapid evolution of SNN algorithms and enables improved software-hardware co-design.

## REFERENCES

- [1] A. Vaswani, N. Shazeer, N. Parmar, J. Uszkoreit, L. Jones, A. N. Gomez, Ł. Kaiser, and I. Polosukhin, “Attention is all you need,” *Advances in neural information processing systems*, vol. 30, 2017.
- [2] A. Radford, J. Wu, R. Child, D. Luan, D. Amodei, I. Sutskever et al., “Language models are unsupervised multitask learners,” *OpenAI blog*, vol. 1, no. 8, p. 9, 2019.
- [3] J. Devlin, M.-W. Chang, K. Lee, and K. Toutanova, “Bert: Pre-training of deep bidirectional transformers for language understanding,” in *Proceedings of the 2019 conference of the North American chapter of the association for computational linguistics: human language technologies, volume 1 (long and short papers)*, 2019, pp. 4171–4186.
- [4] A. Dosovitskiy, L. Beyer, A. Kolesnikov, D. Weissenborn, X. Zhai, T. Unterthiner, M. Dehghani, M. Minderer, G. Heigold, S. Gelly et al., “An image is worth 16x16 words: Transformers for image recognition at scale,” *arXiv preprint arXiv:2010.11929*, 2020.
- [5] L. Yuan, Y. Chen, T. Wang, W. Yu, Y. Shi, Z.-H. Jiang, F. E. Tay, J. Feng, and S. Yan, “Tokens-to-token vit: Training vision transformers from scratch on imagenet,” in *Proceedings of the IEEE/CVF international conference on computer vision*, 2021, pp. 558–567.
- [6] A. Radford, J. W. Kim, C. Hallacy, A. Ramesh, G. Goh, S. Agarwal, G. Sastry, A. Askell, P. Mishkin, J. Clark et al., “Learning transferable visual models from natural language supervision,” in *International conference on machine learning*. PMLR, 2021, pp. 8748–8763.
- [7] W. Maass, “Networks of spiking neurons: the third generation of neural network models,” *Neural networks*, vol. 10, no. 9, pp. 1659–1671, 1997.
- [8] S. Kim, S. Kim, S. Um, S. Kim, J. Lee, and H.-J. Yoo, “Snpu: An energy-efficient spike domain deep-neural-network processor with two-step spike encoding and shift-and-accumulation unit,” *IEEE Journal of Solid-State Circuits*, vol. 58, no. 10, pp. 2812–2825, 2023.
- [9] R. Yin, Y. Li, A. Moitra, and P. Panda, “Mint: Multiplier-less integer quantization for energy efficient spiking neural networks,” in *2024 29th Asia and South Pacific Design Automation Conference (ASP-DAC)*. IEEE, 2024, pp. 830–835.
- [10] Z. Zhou, Y. Zhu, C. He, Y. Wang, S. Yan, Y. Tian, and L. Yuan, “Spikformer: When spiking neural network meets transformer,” *arXiv preprint arXiv:2209.15425*, 2022.
- [11] C. Zhou, L. Yu, Z. Zhou, Z. Ma, H. Zhang, H. Zhou, and Y. Tian, “Spikingformer: Spike-driven residual learning for transformer-based spiking neural network,” *arXiv preprint arXiv:2304.11954*, 2023.
- [12] M. Yao, J. Hu, Z. Zhou, L. Yuan, Y. Tian, B. Xu, and G. Li, “Spike-driven transformer,” *Advances in neural information processing systems*, vol. 36, pp. 64 043–64 058, 2023.
- [13] M. Yao, J. Hu, T. Hu, Y. Xu, Z. Zhou, Y. Tian, B. Xu, and G. Li, “Spike-driven transformer v2: Meta spiking neural network architecture inspiring the design of next-generation neuromorphic chips,” in *The Twelfth International Conference on Learning Representations*, 2024. [Online]. Available: <https://openreview.net/forum?id=1SIBN5Xyw7>
- [14] C. Zhou, H. Zhang, Z. Zhou, L. Yu, L. Huang, X. Fan, L. Yuan, Z. Ma, H. Zhou, and Y. Tian, “Qkformer: Hierarchical spiking transformer using qk attention,” *Advances in Neural Information Processing Systems*, vol. 37, pp. 13 074–13 098, 2024.
- [15] X. Shi, Z. Hao, and Z. Yu, “Spikingresformer: bridging resnet and vision transformer in spiking neural networks,” in *Proceedings of the IEEE/CVF Conference on Computer Vision and Pattern Recognition*, 2024, pp. 5610–5619.
- [16] G. Shen, D. Zhao, T. Li, J. Li, and Y. Zeng, “Are conventional snns really efficient? a perspective from network quantization,” in *Proceedings of the IEEE/CVF Conference on Computer Vision and Pattern Recognition*, 2024, pp. 27 538–27 547.
- [17] G. Shen, D. Zhao, S. Shen, and Y. Zeng, “Enhancing spiking transformers with binary attention mechanisms,” in *The Second Tiny Papers Track at ICLR 2024*, 2024.
- [18] H. Cao, Z. Zhou, W. Wei, A. Belatreche, Y. Liang, D. Zhang, M. Zhang, Y. Yang, and H. Li, “Binary event-driven spiking transformer,” *arXiv preprint arXiv:2501.05904*, 2025.
- [19] H. Liu, Y. Chen, Z. Zeng, M. Zhang, and H. Qu, “A low power and low latency fpga-based spiking neural network accelerator,” in *2023 International Joint Conference on Neural Networks (IJCNN)*. IEEE, 2023, pp. 1–8.
- [20] Y. Chen, W. Ye, Y. Liu, and H. Zhou, “Sibrain: A sparse spatio-temporal parallel neuromorphic architecture for accelerating spiking convolution neural networks with low latency,” *IEEE Transactions on Circuits and Systems I: Regular Papers*, 2024.
- [21] R. Mao, L. Tang, X. Yuan, Y. Liu, and J. Zhou, “Stellar: Energy-efficient and low-latency snn algorithm and hardware co-design with spatiotemporal computation,” in *2024 IEEE International Symposium on High-Performance Computer Architecture (HPCA)*. IEEE, 2024, pp. 172–185.
- [22] R. Yin, Y. Kim, D. Wu, and P. Panda, “Loas: Fully temporal-parallel dataflow for dual-sparse spiking neural networks,” in *2024 57th IEEE/ACM International Symposium on Microarchitecture (MICRO)*. IEEE, 2024, pp. 1107–1121.
- [23] F. Liu, Z. Wang, W. Zhao, N. Yang, Y. Chen, S. Huang, H. Li, T. Yang, S. Pei, X. Liang et al., “Exploiting temporal-unrolled parallelism for energy-efficient snn acceleration,” *IEEE Transactions on Parallel and Distributed Systems*, 2024.
- [24] Y. Gao, T. Wang, Y. Yang, L. Gong, X. Chen, C. Wang, X. Li, and X. Zhou, “Advancing neuromorphic architecture towards emerging spiking neural network on fpga,” *IEEE Transactions on Computer-Aided Design of Integrated Circuits and Systems*, 2025.
- [25] C. Fang, Z. Shen, Z. Wang, C. Wang, S. Zhao, F. Tian, J. Yang, and M. Sawan, “An energy-efficient unstructured sparsity-aware deep snn accelerator with 3-d computation array,” *IEEE Journal of Solid-State Circuits*, 2024.
- [26] A. Gondimalla, N. Chesnut, M. Thottethodi, and T. Vijaykumar, “Sparten: A sparse tensor accelerator for convolutional neural networks,” in *Proceedings of the 52nd Annual IEEE/ACM International Symposium on Microarchitecture*, 2019, pp. 151–165.
- [27] J. Li, G. Shen, D. Zhao, Q. Zhang, and Y. Zeng, “Firefly v2: Advancing hardware support for high-performance spiking neural network with a spatiotemporal fpga accelerator,” *IEEE Transactions on Computer-Aided Design of Integrated Circuits and Systems*, 2024.
- [28] M. T. L. Aung, D. Gerlinghoff, C. Qu, L. Yang, T. Huang, R. S. M. Goh, T. Luo, and W.-F. Wong, “Deepfire2: A convolutional spiking neural network accelerator on fpgas,” *IEEE Transactions on Computers*, vol. 72, no. 10, pp. 2847–2857, 2023.

- [29] Y. Yang, J. S. Emer, and D. Sanchez, "Trapezoid: A versatile accelerator for dense and sparse matrix multiplications," in *2024 ACM/IEEE 51st Annual International Symposium on Computer Architecture (ISCA)*. IEEE, 2024, pp. 931–945.
- [30] P. Dayan and L. F. Abbott, *Theoretical neuroscience: computational and mathematical modeling of neural systems*. MIT press, 2005.
- [31] T. Li, J. Li, G. Shen, D. Zhao, Q. Zhang, and Y. Zeng, "Firefly-s: Exploiting dual-side sparsity for spiking neural networks acceleration with reconfigurable spatial architecture," *IEEE Transactions on Circuits and Systems I: Regular Papers*, 2024.
- [32] A. Parashar, M. Rhu, A. Mukkara, A. Puglielli, R. Venkatesan, B. Khailany, J. Emer, S. W. Keckler, and W. J. Dally, "Scnn: An accelerator for compressed-sparse convolutional neural networks," *ACM SIGARCH computer architecture news*, vol. 45, no. 2, pp. 27–40, 2017.
- [33] Z. Wang, F. Liu, N. Yang, S. Huang, H. Li, and L. Jiang, "Compass: Sram-based computing-in-memory snn accelerator with adaptive spike speculation," in *2024 57th IEEE/ACM International Symposium on Microarchitecture (MICRO)*. IEEE, 2024, pp. 1090–1106.
- [34] S. Panchapakesan, Z. Fang, and J. Li, "Syncnn: Evaluating and accelerating spiking neural networks on fpgas," *ACM Transactions on Reconfigurable Technology and Systems*, vol. 15, no. 4, pp. 1–27, 2022.
- [35] C. S. Wallace, "A suggestion for a fast multiplier," *IEEE Transactions on electronic Computers*, no. 1, pp. 14–17, 1964.
- [36] Y. Zeng, D. Zhao, F. Zhao, G. Shen, Y. Dong, E. Lu, Q. Zhang, Y. Sun, Q. Liang, Y. Zhao *et al.*, "Braincog: A spiking neural network based, brain-inspired cognitive intelligence engine for brain-inspired ai and brain simulation," *Patterns*, vol. 4, no. 8, 2023.
- [37] D. Gerlinghoff, Z. Wang, X. Gu, R. S. M. Goh, and T. Luo, "E3ne: An end-to-end framework for accelerating spiking neural networks with emerging neural encoding on fpgas," *IEEE Transactions on Parallel and Distributed Systems*, vol. 33, no. 11, pp. 3207–3219, 2021.
- [38] P. Dong, M. Sun, A. Lu, Y. Xie, K. Liu, Z. Kong, X. Meng, Z. Li, X. Lin, Z. Fang *et al.*, "Heatvit: Hardware-efficient adaptive token pruning for vision transformers," in *2023 IEEE International Symposium on High-Performance Computer Architecture (HPCA)*. IEEE, 2023, pp. 442–455.
- [39] J. Zhuang, Z. Yang, S. Ji, H. Huang, A. K. Jones, J. Hu, Y. Shi, and P. Zhou, "Ssr: Spatial sequential hybrid architecture for latency throughput tradeoff in transformer acceleration," in *Proceedings of the 2024 ACM/SIGDA International Symposium on Field Programmable Gate Arrays*, 2024, pp. 55–66.
- [40] J. Li, G. Shen, D. Zhao, Q. Zhang, and Y. Zeng, "Firefly: A high-throughput hardware accelerator for spiking neural networks with efficient dsp and memory optimization," *IEEE Transactions on Very Large Scale Integration (VLSI) Systems*, vol. 31, no. 8, pp. 1178–1191, 2023.
- [41] J. Li, T. Li, G. Shen, D. Zhao, Q. Zhang, and Y. Zeng, "Revealing untapped dsp optimization potentials for fpga-based systolic matrix engines," in *2024 34th International Conference on Field-Programmable Logic and Applications (FPL)*. IEEE, 2024, pp. 197–203.
- [42] T. Wang, L. Gong, C. Wang, Y. Yang, Y. Gao, X. Zhou, and H. Chen, "Via: A novel vision-transformer accelerator based on fpga," *IEEE Transactions on Computer-Aided Design of Integrated Circuits and Systems*, vol. 41, no. 11, pp. 4088–4099, 2022.